Hardware Implementation of Quantum Stabilizers in Superconducting Circuits

K. Dodge, Y. Liu, A. R. Klots, B. Cole, A. Shearrow, M. Senatore, S. Zhu, L. B. Ioffe, R. McDermott, and B. L. T. Plourde

Phys. Rev. Lett. **131**, 150602 — Published 13 October 2023

DOI: 10.1103/PhysRevLett.131.150602

Hardware implementation of quantum stabilizers in superconducting circuits

K. Dodge,[1,*] Y. Liu,[1,*] A. R. Klots,[2] B. Cole,[1] A. Shearrow,[3] M. Senatore,[1] S. Zhu,[3] L. B. Ioffe,[2] R. McDermott,[3] and B. L. T. Plourde[1,†]

[1]*Department of Physics, Syracuse University, Syracuse, NY 13244-1130*
[2]*Google Quantum AI, Mountain View, CA*
[3]*Department of Physics, University of Wisconsin-Madison, Madison, Wisconsin 53706*

(Dated: September 11, 2023)

Stabilizer operations are at the heart of quantum error correction and are typically implemented in software-controlled entangling gates and measurements of groups of qubits. Alternatively, qubits can be designed so that the Hamiltonian corresponds directly to a stabilizer for protecting quantum information. We demonstrate such a hardware implementation of stabilizers in a superconducting circuit composed of chains of π-periodic Josephson elements. With local on-chip flux- and charge-biasing, we observe a progressive softening of the energy band dispersion with respect to flux as the number of frustrated plaquette elements is increased, in close agreement with our numerical modeling.

Protecting fragile information in quantum processors requires some form of quantum error correction (QEC). With typical "software" QEC techniques such as the surface code [1], stabilizing a single logical qubit requires many physical qubits, each of which is typically implemented as a weakly nonlinear oscillator. Error correction and computation is achieved by a string of operations and measurements that allow identification of bit-flip and phase-flip errors. An alternative is to implement quantum stabilizers directly in hardware. Here, error correction arises from the natural quantum dynamics, reducing the need for repeated entangling gates, measurements, and a multitude of control lines and complex classical control hardware. In this approach, the highly non-trivial Hamiltonian results in a tiny protected subspace within a huge Hilbert space.

Both approaches can be characterized by the error suppression factor Λ, the rate at which the logical error decreases with system size. The long time required by each round of software error correction for current transmon qubit arrays implies that Λ is only marginally greater than one [2]. In this work, we experimentally demonstrate the potential to achieve much larger $\Lambda \gtrsim 100$ with the Hamiltonian approach. The price that one pays is the appearance of relatively low energy modes with gaps $\lesssim 1$ GHz that make initialization challenging; these gaps can be made higher through parameter optimization. Before building a scalable logical qubit with hardware QEC, it is crucial to demonstrate the effectiveness of protection based on Hamiltonian engineering as system size increases. In this manuscript, we observe and quantify the stabilizing interaction Hamiltonian between unprotected elements. We perform spectroscopic measurements with local flux control and observe signatures of stabilizer terms in the Hamiltonian. Specifically, we find a progressive flattening of the energy bands with respect to flux as system size increases, consistent with linear flux dispersion for a system size of one, quadratic for two, and cubic for three. In addition, we observe a characteristic periodic modulation with offset charge as we tune between regimes with different levels of protection.

A variety of qubit designs with intrinsic protection against decoherence have been studied previously [3, 4], including the 0–π qubit [5–7], the two-Cooper-pair tunneling qubit [8], the bifluxon qubit [9], and rhombi arrays [10–12]. In this last work, previous devices had limited symmetry due to the inability to tune each element to the optimum flux independently; in addition, the devices were sensitive to offset charge fluctuations on internal nodes in each element, and the suppression of tunneling between the logical states was limited. Similar to previous protected qubit designs, our device is based on π-periodic Josephson elements [13], for which the Josephson energy is proportional to $\cos 2\varphi$, where φ is the superconducting phase difference across the element. Here, charge transport consists of coherent tunneling of $4e$, as opposed to $2e$ for a conventional junction. We implement each element as a plaquette formed from a dc Superconducting QUantum Interference Device (SQUID), consisting of two conventional Josephson junctions and a non-negligible loop inductance. When flux-biased at frustration, $\Phi_0/2$ ($\Phi_0 \equiv h/2e$), the first harmonic of the Josephson energy (proportional to $\cos\varphi$) vanishes. This leaves a second order term $E_2 \cos 2\varphi$, with sequential minima separated by π; E_2 depends on the Josephson energy of the individual junctions E_J and the energy of the SQUID inductance E_L (Supplement [19], Sec. XI); φ is thus a compact variable residing on a circle. Biasing below (above) $\Phi_0/2$ raises (lowers) the π wells relative to the 0 wells; for flux bias at $0 \bmod \Phi_0$, the potential becomes proportional to $\cos\varphi$. A small asymmetry between the two junctions has a similar but less severe effect on the $\cos 2\varphi$ potential compared to a small flux deviation from frustration (Supplement [19], Sec. I).

For a single frustrated plaquette with a large capacitive shunt C_{sh} [Fig. 1(a)], tunneling between the ground states in the $0, \pi$ wells is suppressed. In the phase basis,

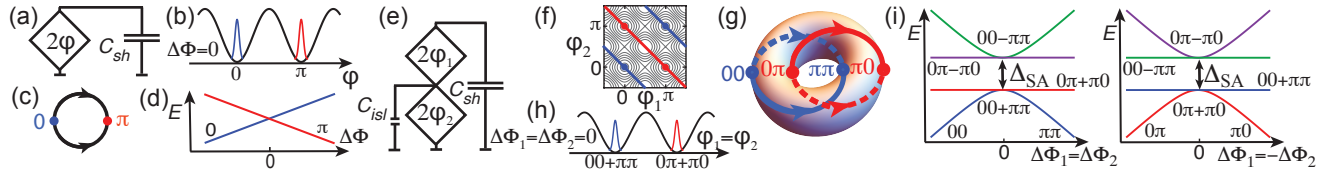

FIG. 1. **Concatenation of π-periodic plaquettes.** (a) Schematic of single plaquette shunted by C_{sh}. (b) $\cos 2\varphi$ potential at frustration ($\Delta\Phi = \Phi - \Phi_0/2 = 0$) with localized wavefunctions in 0 and π wells, drawn in the $0, \pi$ basis for vanishingly small tunneling. (c) Sketch of CW and CCW tunneling paths for φ going between $0,\pi$ wells indicated by blue/red dots. (d) Linear flux dispersion of 0 and π levels for vanishing tunnel splitting. (e) Schematic of two plaquettes shunted by C_{sh} with small capacitance C_{isl} from intermediate island to ground. Potential with respect to phase across each plaquette displayed on (f) contour plot, and (g) surface of torus; blue (red) lines correspond to hybridized even (odd) parity states; arrows indicate CW/CCW tunneling paths between wells of same parity. (h) 1D cut of effective potential at double frustration. (i) Quadratic dispersion of even (odd)-parity levels and flat dispersion of odd (even)-parity levels near double frustration for simultaneous scan of plaquette fluxes along $\Delta\Phi_1 = \Delta\Phi_2$ ($\Delta\Phi_1 = -\Delta\Phi_2$) on left (right) (sketches do not include higher levels within a well).

wavefunctions localized in the $0, \pi$ wells are thus disjoint and well protected against bit-flip errors. At the same time, the wavefunctions are spread out in the charge basis, corresponding for the $0(\pi)$ states to superpositions of even (odd) multiples of Cooper pairs on the logical island where the plaquette connects to C_{sh}. For bias away from frustration, the energy levels disperse linearly [Fig. 1(d)], with no protection against phase flips due to flux noise.

We next consider concatenation of multiple plaquettes while maintaining the large shunt C_{sh} across the array. At double frustration, when two plaquettes are simultaneously biased to $\Phi_0/2$, there are four minima in the two-dimensional surface defined by the phase drops across each plaquette: $00, \pi\pi, 0\pi, \pi 0$. For the two-plaquette circuit this has the topology of a torus, since φ for each plaquette is a compact variable with 2π periodicity [Fig. 1(f,g)]. If the capacitance of the intermediate island between plaquettes to ground C_{isl} is sufficiently small, with charging energy $E_C^{isl} = (2e)^2/2C_{isl} > E_J$, quantum fluctuations of the island phase cause hybridization along the direction between wells of the same parity; that is, 00 will hybridize with $\pi\pi$ and 0π with $\pi 0$. Levels with the same parity develop a splitting near double frustration, with ground states corresponding to the symmetric superpositions $00 + \pi\pi$ ($0\pi + \pi 0$) for even (odd) parity. Excited states are given by the antisymmetric superpositions 00-$\pi\pi$ (0π-$\pi 0$) for even (odd) parity; these states are separated by an energy $\Delta_{\rm SA}$ from the symmetric ground state of the same parity. The hybridized ground state wavefunctions of opposite parity are the logical states for the device [Fig. 1(h)] and form interlocking rings on the torus [Fig. 1(g)]. Due to delocalization and intertwining of the hybridized ground state wavefunctions, local perturbations affect the logical states symmetrically. Larger E_C^{isl} increases $\Delta_{\rm SA}$ and further flattens the bands [Fig. 1(i)], thus protecting against dephasing from flux noise.

Treating each plaquette as a spin-1/2 particle, the $\Delta_{\rm SA}$ splitting corresponds to an XX stabilizer term in the Hamiltonian of frustrated plaquettes i, j: $H_{XX} = -(\Delta_{\rm SA}^{(ij)}/2) X_i X_j$, where X_i is the Pauli σ_x matrix for plaquette i. The error suppression factor Λ can be approximated as the ratio of $\Delta_{\rm SA}^{(ij)}$ to twice the scale h_Z of dephasing fluctuations for single plaquette i, $\delta H(t) = h_Z(t) Z_i$, which, for this device, will be dominated by flux noise (Supplement [19], Sec. XII). C_{sh} still suppresses tunneling between logical states of opposite parity, protecting against bit-flip errors.

In our experiments, we target a three-plaquette circuit with $E_J \sim E_L \sim 1.5\,\mathrm{K}$ (k_B=1), where E_L is the energy $(\Phi_0/2\pi)^2/L$ of the inductance L on each plaquette arm. We aim for a charging energy of each plaquette junction $E_C = (2e)^2/2C_j \sim 3.5\,\mathrm{K}$, where C_j is the junction capacitance. These values can be achieved with conventional Al-AlO_x-Al junctions. We implement the inductors with chains of large-area junctions, similar to fluxonium [22], thus eliminating charge fluctuations on the internal nodes between each small junction and inductor within a plaquette. The shunt capacitor C_{sh}=1.2 pF is capacitively coupled to a resonator. There are four flux-bias lines, each of which couples strongly to one or two plaquettes. There are three charge-bias lines: one to the logical island that forms C_{sh}, and one to each intermediate island between plaquettes (Supplement [19], Sec. II-V).

For device tune-up, we scan various pairs of flux-bias lines while monitoring the dispersive shift of the readout resonator. Each blue line in Fig. 2(a,b) corresponds to one plaquette passing through frustration. A crossing of two (three) lines indicates double (triple) frustration. The spacing between parallel sets of lines defines the period Φ_0. We fit the slopes and spacing of the lines to extract the inductance matrix mapping bias levels on each flux line to net flux coupled to each plaquette (Supplement [19], Sec. VI). By inverting this matrix, we determine bias parameters for moving along arbitrary flux vectors.

We next map out the flux dispersion of the level transitions for different frustration conditions. With our abil-

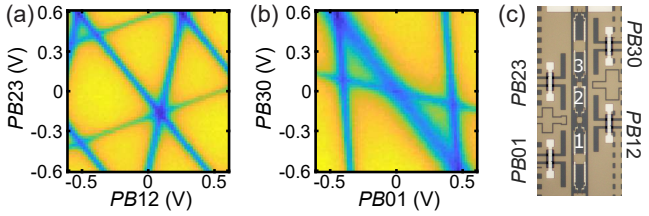

FIG. 2. **Multi-plaquette flux biasing.** 2D flux-modulation scans of readout cavity dispersive shift for (a) $PB23$ vs. $PB12$, (b) $PB30$ vs. $PB01$. (c) Optical micrograph of device.

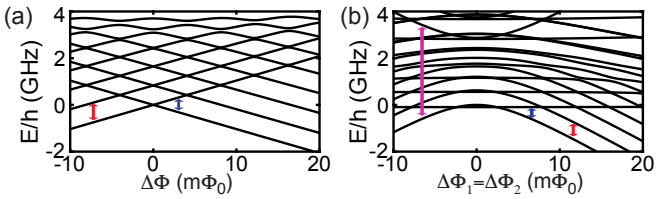

FIG. 3. **Level transitions.** Simulated level diagrams near (a) single and (b) double frustration; lines indicate example plasmons (red), heavy fluxons (blue), light fluxons (magenta).

ity to adjust the various plaquette fluxes independently using local flux-biasing, we maintain some plaquettes at unfrustration ($0 \bmod \Phi_0$), where the plaquette behaves like a conventional Josephson element, while we scan the flux of other plaquettes near frustration. In Fig. 3, we consider the expected level structure and define the types of possible transitions. We refer to transitions between levels in the same well as *plasmons*; transitions between different wells are referred to as *heavy fluxons* because of the vanishingly small gap associated with the corresponding anticrossing, a consequence of the large effective mass from C_{sh}. Transitions between hybridized levels of the same parity but opposite symmetry, for example, $00{+}\pi\pi$ to $00{-}\pi\pi$, disperse sharply with flux; these are known as *light fluxons* due to the low effective mass in the $\varphi_2 = -\varphi_1$ direction from the smallness of C_{isl}.

To perform spectroscopy, we drive a microwave probe tone into the charge bias line coupled to C_{sh} while monitoring the cavity dispersive shift. Near single frustration, we initialize in the π well prior to each spectroscopy pulse by setting the bias to $0.1\,\Phi_0$ from frustration, thus moving out of the protected space; we then quickly ramp the bias to the measurement point and apply spectroscopy and readout pulses (Supplement [19], Sec. VII). In Fig. 4(a), we show single-frustration measurements for plaquette 2. Features that disperse gradually correspond to plasmons within the π well where the qubit is initialized. We continue to observe transitions out of the π well even when the device is biased past frustration, where the π well is higher in energy than the 0 well, due to suppressed tunneling between states of opposite parity. In addition to the 0-1, 0-2, and 0-3 transitions, we observe transitions out of excited states in the well, such as 1-2, 1-3, and 1-4, and even 2-3 and 2-4, due to insufficient cooling into the ground state of the π well. Because of the spurious excitations to multiple levels, we are unable to apply initialization techniques that are commonly used for other low-gap qubits, such as heavy fluxonium [15, 16]. Nevertheless, we observe only weak transitions out of the 0 well, indicating that we are predominantly preparing the circuit in the π well. In addition to the plasmons, we also observe heavy fluxons that disperse linearly with flux, which arise from transitions between various levels in the π and 0 wells, where the barrier to tunneling is small because the initial state is an excited level or the wells are tilted by the flux bias; note that we do not observe the heavy fluxon between the protected ground states in the 0 and π wells, which are the logical levels. We observe similar behavior for plaquettes 1 and 3 (Supplement [19], Sec. X).

The curves included in Fig. 4(a) are generated from detailed numerical modeling of the device energy levels (Supplement [19], Sec. IX). With the ability to calculate the level spectrum, we adjust the circuit parameters to fit the measured transitions from the spectroscopic data (Supplement [19], Sec. X). We observe excellent agreement, even capturing splittings that result when a fluxon crosses a plasmon due to resonant tunnel coupling between aligned levels in the 0 and π wells. In addition, these splittings depend on the offset charge on the C_{sh} island [Fig. 4(e)] due to Aharonov-Casher (A-C) interference [17, 18] between tunneling paths clockwise (CW) or counterclockwise (CCW) in the $\cos 2\varphi$ potential [Fig. 1(c)] (Supplement [19], Sec. VIII). At single frustration, as expected, the heavy fluxon dispersion is linear down to zero energy, thus offering no protection against flux noise.

Upon tuning to double frustration, we observe a qualitatively different behavior. We initialize in the $\pi\pi$ well of the two-plaquette potential, then quickly ramp near double frustration. We scan both plaquette fluxes in tandem along the direction between the regimes with a global potential minimum at $\pi\pi$ and 00 and passing through double frustration. Spectroscopy at plaquette (12) double frustration shows plasmons similar to the single frustration measurements [Fig. 4(b)]. However, unlike single frustration, where suppressed tunneling between the $0, \pi$ wells allows the device to remain in the π well even after the flux is ramped well past frustration, at double frustration, the large symmetric-antisymmetric gap $\Delta_{\mathrm{SA}}^{(12)}$ causes an adiabatic transition from $\pi\pi$ to 00 upon passing through double frustration. At higher frequencies, we observe steeply dispersing light fluxons, with the minimum at double frustration corresponding to $\Delta_{\mathrm{SA}}^{(12)}$ from hybridization of the 00 and $\pi\pi$ wells. For scans along the odd-parity flux direction, or if the circuit is initialized in

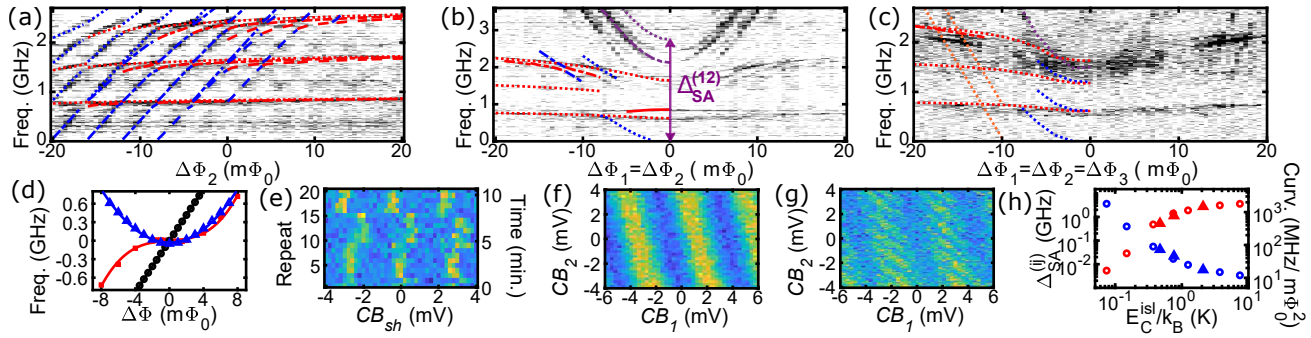

FIG. 4. **Spectroscopy at different frustration points.** Spectroscopy at (a) plaquette 2 single frustration, (b) plaquette (12) double frustration, and (c) triple frustration. Lines indicate modeled transitions with: red = plasmons, blue = heavy fluxons, purple = light fluxons, dotted = transitions out of 0 level, dash-dotted = transitions out of 1 level, dashed = transitions out of 2 level, solid red line = plasmon transition between antisymmetric levels in even-parity well, orange = light fluxon plus cavity photon (Supplement [19], Sec. X). (d) Comparison of dispersion of lowest heavy fluxon from modeled levels with linear, quadratic, and cubic fits for single (black circle), double (blue triangle), and triple (red square) frustration; frequency axis inverted for single and triple frustration for $\Delta\Phi < 0$. (e) Repeated scans of cavity response vs. offset charge bias to C_{sh} island at plaquette 2 single frustration. 2D scan of spectroscopy at 0-1 transition frequency while scanning bias voltages to gate electrodes coupled to both intermediate islands for (f) plaquette (12) double frustration and (g) triple frustration. (h) Plot of $\Delta_{\mathrm{SA}}^{(ij)}$ and curvature of fluxon transition between even/odd-parity ground states vs. E_C^{isl} showing measured values for plaquette (12), (23), and (13) double frustration (solid triangles) plus modeled values for a range of C_{isl} (open circles).

an odd-parity well and scanned in the even-parity flux direction, the spectral features become swapped [Fig. 1(i), Supplement [19], Sec. X.C].

As with spectroscopy at single frustration, we include curves for the various transitions from numerical modeling and fitting for double frustration [Fig. 4(b)]. Here, the larger Hilbert space requires a significant increase in computational resources. Our modeled transition curves agree well with the measured spectroscopy, capturing both the plasmons and heavy fluxons. We are unable to directly drive a microwave transition between the logical states in the $00{+}\pi\pi$ and $0\pi{+}\pi0$ wells due to the vanishing matrix element, the basis of protection. However, the increasing flatness of the higher fluxon transitions as one moves lower in the spectrum indicates that the logical levels will be the flattest. This can also be seen in the blue modeled curves near the bottom of the figure highlighting the dispersion of the logical level transition, which exhibits quadratic curvature. Additionally, our modeling captures the light fluxons to the antisymmetric levels.

The effectiveness of concatenation depends on C_{isl} of the intermediate island between the two frustrated plaquettes. For plaquette (12) double frustration, $\Delta_{\mathrm{SA}}^{(12)}$ is 2.7 GHz. At plaquette (23) double frustration, which involves a significantly larger C_{isl} because of the orientation of the plaquette 2 inductors, we observe a smaller $\Delta_{\mathrm{SA}}^{(23)}$ and a correspondingly larger curvature of the heavy fluxon transition. $\Delta_{\mathrm{SA}}^{(13)}$ is even smaller because of the excess capacitance to ground of the unfrustrated plaquette 2 (Supplement [19], Sec. X). Figure 4(h) shows the variation of Δ_{SA} with E_C^{isl}, including measured values of $\Delta_{\mathrm{SA}}^{(ij)}$ for each combination of double frustration, as well as numerically modeled values. For a typical flux noise level, h_Z for these plaquettes will be $\sim$2 MHz, which, when combined with the measured $\Delta_{\mathrm{SA}}^{(12)}$, is consistent with $\Lambda \sim 700$. Note that this is an extracted parameter characterizing protection in one channel: dephasing. The complete Λ-parameter for a logical qubit must be derived from the scaling of T_1 and T_2 with system size, which is beyond the scope of this manuscript. Nonetheless, Λ can also be expressed as the ratio of T_2 for a higher degree of frustration relative to T_2 at single frustration (Supplement [19], Sec. XII).

In addition to the symmetric/antisymmetric gap, another characteristic of the stabilizer term is the periodic modulation of $\Delta_{\mathrm{SA}}^{(ij)}$ with offset charge on the intermediate island between plaquettes i and j. Destructive A-C interference of tunneling paths in the CW and CCW directions on the constant-parity circles for double frustration [Fig. 1(g)] causes $\Delta_{\mathrm{SA}}^{(ij)}$ to vanish for island offset charge near $e \bmod 2e$. We observe periodic modulation with charge bias to the islands with a spectroscopy pulse on the 0-1 transition [Fig. 4(f)]. While the island offset charge is stable on timescales up to one hour, it is critical there are no jumps to near $e \bmod 2e$. Thus, it is important to actively stabilize these offset charges through periodic calibrations (Supplement [19], Sec. VIII, IX).

By simultaneously frustrating all plaquettes, we measure spectroscopy near triple frustration [Fig. 4(c)]. In this case, we are unable to numerically fit the level spectrum since the Hilbert space size becomes prohibitively large. Nonetheless, we are able to compute the spectrum using parameter values from previous fits to double and single frustration, although the calculation takes sev-

eral weeks to complete. We obtain reasonable agreement with the measurements, although the spectral features are more challenging to resolve compared to other degrees of frustration; the higher transitions are off by ∼5-10%, which is not unreasonable considering the circuit complexity and intertwined wavefunctions, given limitations on the number of quantum states needed for the computation to converge. Around 1.5 GHz, we observe a prominent central flat feature of width ∼7 mΦ_0 around the 0-3 transition, which is uncharacteristic for parabolic, let alone linear, dispersion; below this, the 0-1 transition around 0.6 GHz is similarly flat. The transition between the logical states, which cannot be directly driven due to protection of these states from the environment, will be comparably flat (Supplement [19], Sec. X.D). Also, the light fluxon transitions are qualitatively different compared to double frustration. We additionally observe charge modulation with two different periods and slopes corresponding to separate tuning of offset charge on each intermediate island [Fig. 4(g)], characteristic of a Hamiltonian with two stabilizer terms: $H_{XX} = -(\Delta_{\mathrm{SA}}^{(12)}/2)X_1X_2 - (\Delta_{\mathrm{SA}}^{(23)}/2)X_2X_3$. For our present device $\Delta_{\mathrm{SA}}^{(23)}$ is smaller than $\Delta_{\mathrm{SA}}^{(12)}$ due to excess ground capacitance from plaquette 2, resulting in the logical level dispersion at triple frustration being only marginally flatter than at double frustration [Fig. 4(d)] (Supplement [19], Sec. XI).

While our present device successfully demonstrates the implementation of stabilizer terms in hardware, development of protected qubits based on hybridized ground states of opposite parity requires larger gaps to the excited states. This, in conjunction with weaker radiative coupling to parasitic high-frequency modes from a more compact C_{sh}, perhaps achieved using a parallel-plate rather than planar design, will avoid spurious excitations to multiple excited levels that complicate the initialization process for our present device. A device with higher excited-state energies that can be operated in the qubit regime requires larger E_J, ideally at least 3 K. We must also maintain even larger E_C to have large Δ_{SA} at double frustration with the resulting flat dispersion. For a qubit with these improved parameters subject to typical flux- and charge-noise levels, optimistic but feasible junction asymmetries, and dielectric loss from a parallel-plate C_{sh}, we project $\Lambda \gtrsim 100$, corresponding to $T_1 \gg 1\,\mathrm{s}$ and $T_2 \sim 60\,\mathrm{ms}$ (Supplement [19], Sec. XI), well beyond current state-of-the-art superconducting qubits.

This work is supported by the U.S. Government under ARO grant W911NF-18-1-0106. Fabrication was performed in part at the Cornell NanoScale Facility, a member of the National Nanotechnology Coordinated Infrastructure (NNCI), which is supported by the National Science Foundation (Grant NNCI-2025233). Portions of this work were supported by the National Science Foundation, Quantum Leap Challenge Institute for Hybrid Quantum Architectures and Networks, Grant No. 2016136.

* These authors contributed equally
† bplourde@syr.edu

[1] A. G. Fowler, M. Mariantoni, J. M. Martinis, and A. N. Cleland, Physical Review A **86**, 032324 (2012).
[2] Google Quantum AI, Nature **595**, 383 (2021).
[3] B. Douçot and L. B. Ioffe, Reports on Progress in Physics **75**, 072001 (2012).
[4] A. Gyenis, A. Di Paolo, J. Koch, A. Blais, A. A. Houck, and D. I. Schuster, PRX Quantum **2**, 030101 (2021).
[5] P. Brooks, A. Kitaev, and J. Preskill, Phys. Rev. A **87**, 052306 (2013).
[6] P. Groszkowski, A. Di Paolo, A. Grimsmo, A. Blais, D. I. Schuster, A. A. Houck, and J. Koch, New Journal of Physics **20**, 043053 (2018).
[7] A. Gyenis, P. S. Mundada, A. Di Paolo, T. M. Hazard, X. You, D. I. Schuster, J. Koch, A. Blais, and A. A. Houck, PRX Quantum **2**, 010339 (2021).
[8] W. C. Smith, A. Kou, X. Xiao, U. Vool, and M. H. Devoret, npj Quantum Information **6**, 1 (2020).
[9] K. Kalashnikov, W. T. Hsieh, W. Zhang, W.-S. Lu, P. Kamenov, A. Di Paolo, A. Blais, M. E. Gershenson, and M. T. Bell, PRX Quantum **1**, 010307 (2020).
[10] L. B. Ioffe, M. V. Feigel'man, A. Ioselevich, D. Ivanov, M. Troyer, and G. Blatter, Nature **415**, 503 (2002).
[11] S. Gladchenko, D. Olaya, E. Dupont-Ferrier, B. Douçot, L. B. Ioffe, and M. E. Gershenson, Nature Physics **5**, 48 (2009).
[12] M. T. Bell, J. Paramanandam, L. B. Ioffe, and M. E. Gershenson, Physical Review Letters **112**, 167001 (2014).
[13] W. C. Smith, M. Villiers, A. Marquet, J. Palomo, M. R. Delbecq, T. Kontos, P. Campagne-Ibarcq, B. Douçot, and Z. Leghtas, Physical Review X **12**, 021002 (2022).
[22] V. E. Manucharyan, J. Koch, L. I. Glazman, and M. H. Devoret, Science **326**, 113 (2009).
[15] D. Gusenkova, M. Spiecker, R. Gebauer, M. Willsch, D. Willsch, F. Valenti, N. Karcher, L. Grünhaupt, I. Takmakov, P. Winkel, et al., Physical Review Applied **15**, 064030 (2021).
[16] U. Vool, A. Kou, W. C. Smith, N. E. Frattini, K. Serniak, P. Reinhold, I. M. Pop, S. Shankar, L. Frunzio, S. M. Girvin, and M. H. Devoret, Physical Review Applied **9**, 054046 (2018).
[17] Y. Aharonov and A. Casher, Physical Review Letters **53**, 319 (1984).
[18] M. T. Bell, W. Zhang, L. B. Ioffe, and M. E. Gershenson, Physical Review Letters **116**, 107002 (2016).
[19] See Supplemental Material [URL `willbeinteredbyPRL`] for further details of the device design, fabrication, measurements, data analysis, and numerical modeling, which includes Refs. [20–35].
[20] V. Lefevre-Seguin, E. Turlot, C. Urbina, D. Esteve, and M. H. Devoret, Physical Review B **46**, 5507 (1992).
[21] J. Mooij, T. Orlando, L. Levitov, L. Tian, C. H. Van der Wal, and S. Lloyd, Science **285**, 1036 (1999).
[22] V. E. Manucharyan, J. Koch, L. I. Glazman, and M. H. Devoret, Science **326**, 113 (2009).

[23] J. Koch, T. M. Yu, J. Gambetta, A. A. Houck, D. I. Schuster, J. Majer, A. Blais, M. H. Devoret, S. M. Girvin, and R. J. Schoelkopf, Physical Review A **76**, 042319 (2007).
[24] U. Eckern, G. Schön, and V. Ambegaokar, Physical Review B **30**, 6419 (1984).
[25] InductEx, SUN Magnetics.
[26] B. Foxen, J. Mutus, E. Lucero, E. Jeffrey, D. Sank, R. Barends, K. Arya, B. Burkett, Y. Chen, Z. Chen, et al., Superconductor Science and Technology **32**, 015012 (2018).
[27] M. A. Rol, L. Ciorciaro, F. K. Malinowski, B. M. Tarasinski, R. E. Sagastizabal, C. C. Bultink, Y. Salathe, N. Haandbæk, J. Sedivy, and L. DiCarlo, Applied Physics Letters **116**, 054001 (2020).
[28] ANSYS, ANSYS Q3D Extractor.
[29] B. G. Christensen, C. D. Wilen, A. Opremcak, J. Nelson, F. Schlenker, C. H. Zimonick, L. Faoro, L. B. Ioffe, Y. J. Rosen, J. L. DuBois, B. L. T. Plourde, R. McDermott, Physical Review B **100**, 140503(R) (2019).
[30] C. Wilen, S. Abdullah, N. Kurinsky, C. Stanford, L. Cardani, G. d'Imperio, C. Tomei, L. Faoro, L. Ioffe, C. Liu, et al., Nature **594**, 369 (2021).
[31] O. Rafferty, S. Patel, C. Liu, S. Abdullah, C. Wilen, D. Harrison, and R. McDermott, arXiv preprint arXiv:2103.06803 (2021).
[32] C.-H. Liu, D. C. Harrison, S. Patel, C. D. Wilen, O. Rafferty, A. Shearrow, A. Ballard, V. Iaia, J. Ku, B. Plourde, et al., arXiv preprint arXiv:2203.06577 (2022).
[33] A. R. Klots, *SuperQuantPackageV2* (2022), [Online; accessed 6. Jul. 2022], URL https://github.com/andreyklots/SuperQuantPackageV2.
[34] A. D. O'Connell, M. Ansmann, R. C. Bialczak, M. Hofheinz, N. Katz, E. Lucero, C. McKenney, M. Neeley, H. Wang, E. M. Weig, et al., Appl. Phys. Lett. **92**, 112903 (2008), ISSN 0003-6951.
[35] O. Astafiev, Y. A. Pashkin, Y. Nakamura, T. Yamamoto, and J.-S. Tsai, Physical Review Letters **96**, 137001 (2006).